Plasmonics
https://doi.org/10.1007/s11468-024-02319-z

RESEARCH

A Simple Structure of High Sensitivity of Plasmonic Photonic Crystal Fiber Sensors with Minimal Air Hole Density in Fiber Cladding

Chung-Ting Chou Chao[1] · Minhaz Uddin Ahmed[2] · Hung Ji Huang[3] · Chee Ming Lim[4] · Muhammad Raziq Rahimi Kooh[4] · Roshan Thotagamuge[5] · Yuan-Fong Chou Chau[4]

Received: 20 March 2024 / Accepted: 17 April 2024

Abstract

Surface plasmon resonance (SPR)-based photonic crystal fiber (PCF) sensors have advanced significantly in recent years, yet many proposed sensors suffer from low sensitivity or complex fabrication processes that use many air holes in fiber cladding that are unsuitable for real-time applications. To address this, we propose and analyze a reduced air hole of the SPR-PCF with only four circular air holes in the cladding. This design choice simplifies fabrication and reduces costs compared to a sensor with a larger number of air holes. Using the finite element method (FEM), we demonstrate that our sensor achieves a maximum sensitivity of 11,000 nm/RIU along with the figure of merit of 220 1/RIU and a maximum theoretical resolution (MTR) of 9.09×10^{-6} RIU (RIU refers to the refractive index unit) using the wavelength interrogation technique. We believe that the designed SPR-PCF sensor holds promise for detecting biomolecular and biological analyte because of its high sensitivity and simple structure. Notably, the smaller number of air holes in our design produces greater sensitivity than previously reported work that uses more air holes in the fiber cladding. To our knowledge, this represents the lowest number of circular air holes used in PCF fiber cladding for refractive index sensing, highlighting our proposed sensor design's novel and practical approach.

Keywords Sensitivity · Resolution · PCF · Plasmonics · Sensor · FEM

Introduction

Given its unique optical properties and its ability to solve the diffraction limit, the influence of surface plasmon resonance (SPR) on the interface between plasmonic materials and dielectrics has attracted considerable interest among researchers [1–3]. The characteristic for the SPR is the coherent oscillation of electrons on the surface of plasma materials, generating localized SPR and propagating surface plasmon (SPP) forms of SPR [4–6]. These phenomena are integral at the design of nanophotonic devices, particularly in sensing and detection applications [7–9].

Photonic crystal fibers (PCFs) utilize air holes to lower the fiber-cladding's effective refractive index (RI), enabling total internal reflection within waveguide. The lattice pattern of air holes endows PCFs with a wide range of optical behaviors that are not achievable with conventional optical fibers [10–12]. In particular, PCFs can manipulate light in various ways, including guiding specific modes, enabling broadband transmission, exhibiting modal birefringence, and facilitating nonlinear optical effects [13, 14].

✉ Roshan Thotagamuge
roshan@wyb.ac.lk

✉ Yuan-Fong Chou Chau
chou.fong@ubd.edu.bn

1 King Yuan Electronics Co., LTD., No. 81, Section 2, Gongdaowu Road, Hsin-Chu 300, Taiwan, R. O. C.

2 Biosensor and nanobiotechnology Laboratory, Integrated Science Building, Faculty of Science, 6 Universiti Brunei Darussalam, Jalan Tungku Link, Gadong BE1410, Darussalam, Brunei

3 Department of Electro-Optical Engineering, National Formosa University, Yunlin 632, Taiwan

4 Centre for Advanced Material and Energy Sciences, Universiti Brunei Darussalam, Tungku Link, Gadong BE1410, Brunei, Darussalam

5 Department of Nano Science Technology, Faculty of Technology, Wayamba University of Sri Lanka, Kuliyapitiya 60200, Sri Lanka

Published online: 08 May 2024

Incorporating SPR and SPP effects into PCFs enhances their performance in sensing applications. SPR-PCF sensors, achieved of coating metal layers or nanoparticles on the PCF surface, exhibit remarkable sensitivity to changes are expected in RI near the fiber surface. This sensitivity enables label-free detection, real-time monitoring, and compatibility with diverse analytes, making them highly versatile in various sensing scenarios. In recent years, there has been a growing interest in SPR-PCF-based sensors because of their ability to control the coupling energy between the fiber and the surrounding medium under test [15]. For instance, Dandapat et al. demonstrated the biomolecule sensing capacity of such sensors by the calculating the adlayer/surface sensitivity [16, 17]. The integration of plasmonic materials with PCF technology to construct SPR-PCF-based sensors offers significant advantages, including design and compact dimensions [18–21]. This combination allows for tailored sensor designs that can be adapted to specific application requirements while maintaining compact form factors suitable for various deployment scenarios.

The mechanism of the SPR-PCF sensor is based on the principle of SPR coupled with the testing medium. As light propagates through the PCF, it interacts with the air holes in fiber cladding. Metal coatings or nanoparticles placed onto the PCF surface selectively enhance the evanescent field near the fiber surface. The sensor operates through evanescent electromagnetic (EM) interaction with plasmonic nanometals. When the sensor is exposed to an analyte with an RI close to the metal's dielectric constant, SPRs are excited at the metal–dielectric interface, leading to changes in PCF's optical properties, such as shifts in resonance wavelengths or intensity variations. By monitoring these changes, the SPR-PCF sensor can detect and quantify RI variations in the surrounding medium with high sensitivity and specificity [22, 23]. Electromagnetic waves penetrate the fiber cladding region, generating evanescent electromagnetic waves that excite the free electrons on the surface of nanometals, producing SPP waves at the metal–dielectric interface [24–28]. At resonance wavelength, the effective RI part of the core-guided mode and the SPP mode perfectly match phase, resulting in sharp confinement loss (CL) peaks, which can detect unknown samples/analytes [29–31].

Increasing the number of air holes in the PCF cladding lowers its equivalent RI, while decreasing the number of air holes increases the equivalent RI of the cladding area. The properties of PCF are closely dependent on the number and arrangement of air holes in the fiber cladding. The number of circular air holes used in the SPR-PCF sensor directly affects the CL experienced by the guided modes within the fiber. Increasing the number of air holes typically leads to higher CL because of the increased interaction between the guided modes and the surrounding air holes. This increase in CL can affect the sensor's overall performance by the influence of transmission properties and sensitivity to changes in RI. Therefore, careful optimization of the number and arrangement of air holes is essential to balance the trade-off between CL and sensor performance in SPR-PCF sensors.

Various design strategies have been proposed in recent years using the different values of arrangements and amounts of air holes placed in PCF cladding. Li et al. [32] introduced a D-shaped PCF sensor employing 43 circular air holes and one elliptical air hole in the fiber cladding, achieving an average RI sensitivity of 12,167 nm/RIU within the range of 1.26 to 1.32. Majeed et al. [33] developed a dual open microchannel SPR-PCF RI sensor using 60 rectangular air holes in the PCF, achieving a sensitivity of 33,000 nm/RIU in the RI range of 1.37 to 1.43 and a maximum resolution of 5.56×10^{-6} RIU. Chang et al. [34] designed an SPR-PCF sensor with 36 air holes, achieving a CL of 442 dB/cm for y-polarized mode. Rifat et al. [35] proposed a plasmonic PCF sensor with 37 air holes, obtaining a maximum sensitivity of 3,000 nm/RIU in the RI range of 1.46 to 1.49. Although SPR-PCF sensors demonstrate high RI sensitivity, their structures involve numerous air holes (more than 36), increasing fabrication complexity and production costs.

In this study, we introduce a simplified sensor structure with a PCF surface coated with an Au layer and only four half-circular circular air holes, which can detect analytes externally. We inspect the sensitivity of this device using the COMSOL Multiphysics software based on the finite element method (FEM). Our investigation reveals that structural parameters, such as the air hole size and thickness of the plasmonic material (Au), significantly influence the full width at half maximum (FWHM) and the CL amplitude. Md. Saiful Islam et al. [36] designed a biosensor using a configuration with four truncated air holes, while our work utilizes a structure with four perfectly circular air holes in the fiber cladding. It is crucial to highlight several key distinctions between our study and the work of ref. [36]. First, in their study, four air holes are incorporated into the fiber cladding, but their edges are partially truncated, which complicates the fabrication process of the SPR PCF. This complication arises because the truncated edges lack a surface for the Au film to adhere to, making it difficult to form air holes in the fiber cladding. Additionally, this may potentially affect precision. In contrast, our research employs a configuration with four complete air holes in the fiber cladding, facilitating the coating of the Au film on the outer layer and reducing fabrication challenges. Second, while both studies employ a PCF design with minimal air hole density in the cladding region, our research focuses specifically on investigating the sensitivity to SPR for sensing applications. We provide a comprehensive exploration of SPR sensing performance and provide information on potential applications, thus extending the scope beyond mere design similarity. Third, our numerical investigation delves into detailed electromagnetic behavior,

encompassing analysis of field distributions, mode profiles, and sensitivity enhancements. This in-depth analysis contributes to a better understanding of the underlying mechanisms governing SPR sensing in PCF structures with minimal air hole density, thus adding depth to the field of study. Furthermore, while the work by ref. [36] provides flexibility in providing valuable information on exposed core localized SPR biosensors; our study expands the research landscape by focusing on a different PCF configuration. By emphasizing the significance of minimal air hole density for achieving high sensitivity in SPR sensing applications, we contribute to advancing the field. In summary, our research offers a thorough investigation into the SPR sensing performance of a simple PCF design with minimal air hole density. We believe that our study provides valuable insight and lays the groundwork for further advancements in plasmonic photonic crystal fiber sensors.

The novelty of our proposed SPR-PCF sensor lies in its superior sensing performance, characterized by higher sensitivity and better resolution, achieved with the fewest air holes in the fiber cladding. To the best of our knowledge, our sensor design incorporates the most minor air holes compared to reported articles in the literature. Our results establish an experimental foundation and provide theoretical insights for the development of high-sensitivity SPR-PCF sensors, demonstrating that our designed structure exhibits superior sensing performance with higher sensitivity and better resolution while utilizing the least number of air holes in the fiber cladding.

Simulation Models and Principles

Large-diameter circular air holes are more uncomplicated to process in the fabrication of PCFs than small-diameter air holes. Additionally, circular air holes are more accessible to manufacture than elliptical air holes in fabrication. For simplicity in fabricating the fiber structure and considering cost, we opt for a configuration with four larger circular air holes in the PCF cladding, as illustrated in Fig. 1. This figure presents a schematic diagram of the designed SPR-PCF-based sensor. To improve birefringence [37–39], we employed two sizes of circular air holes in the fiber cladding, denoted by radii r_1 and *r2,*. Their coordinates are ($\pm d_1$,

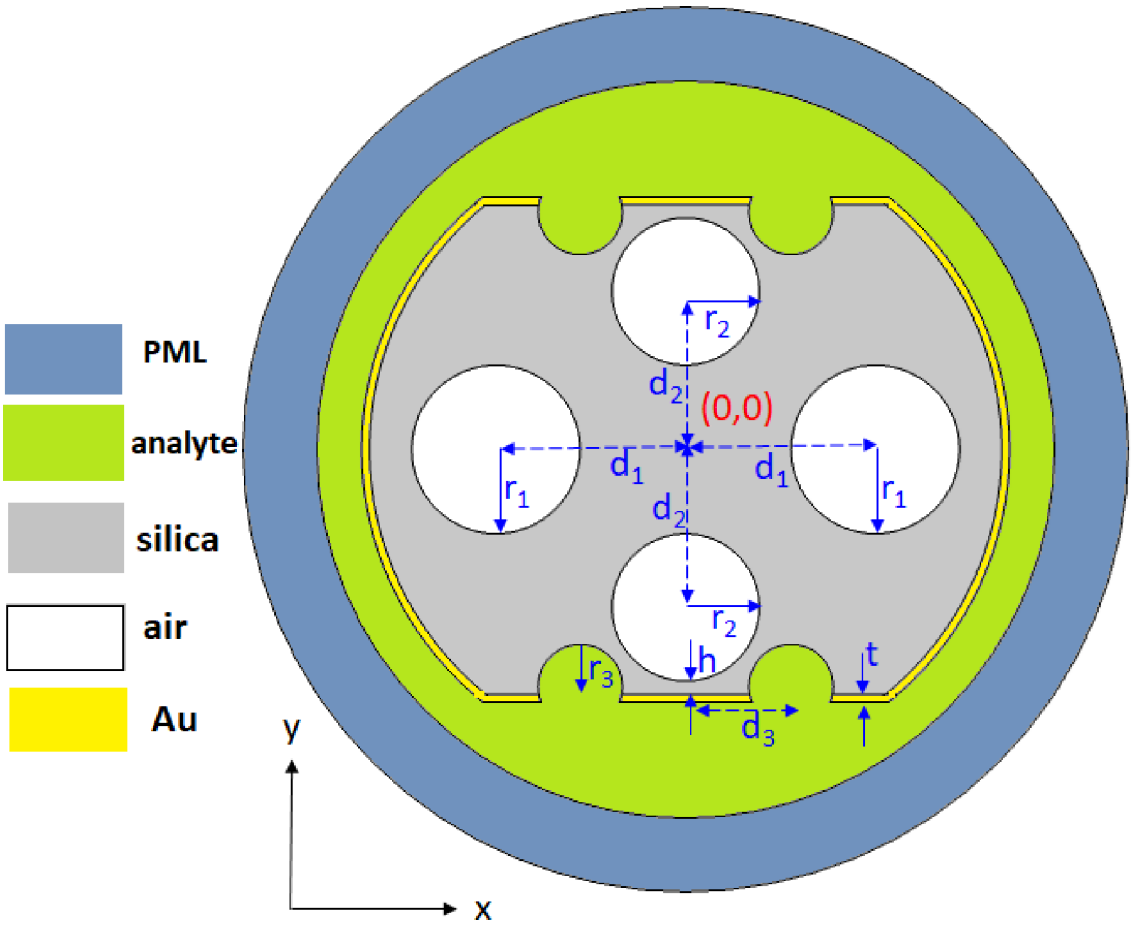

Fig. 1 Schematic diagram of the designed SPR PCF-based sensor with structure parameters

0) along the x-axis for the larger holes and $(0, \pm d_2)$ along the y-axis for the smaller ones. Furthermore, four uncoated curves with a radius of r_3, are placed at the fiber boundary $(\pm d3 \pm (d_2 + r_2 + h))$. The reason to not coat the Au film on the surface of the four half-circular curves was to maintain the open windows, which facilitated the coupling effect between the fiber core mode and the analyte under testing [40].

A gold (Au) film coats the flat surfaces of the top and bottom surfaces and the fiber's outer surface, enhancing the SPR-PCF sensor's detection capability. The analyte (thickness 0.5 µm) under test surrounds the entire fiber structure and consists of liquids with different refractive indices in the range of $n = 1.30$–1.385, where n represents RI. Changes in RI (Δn) result in variations in resonance wavelength ($\Delta\lambda_{res}$), enabling the detection of changes in RI. Numerical simulations were conducted using COMSOL Multiphysics, with scattering boundary conditions and perfectly matched layer boundary conditions added in the external computational domain to absorb reflections at the boundaries. A finer mesh of 17,576 domain elements and 1,574 boundary elements was used.

A fused silica material with a diameter of 6 µm diameter serves as a representation of the core and cladding regions. The RI of this material is determined using the Sellmeier equation [41]:

$$n^2(\lambda) = 1 + \frac{B_1\lambda^2}{\lambda^2 - C_1} + \frac{B_2\lambda^2}{\lambda^2 - C_2} + \frac{B_3\lambda^2}{\lambda^2 - C_3} \quad (1)$$

In Eq. (1), n and λ denote RI and wavelength (in units of µm). $B_1 = 0.696163$, $B_2 = 0.4079426$, $B_3 = 0.987479400$, $C_1 = 0.0046791486$, $C_2 = 0.0135120631$, and $C_3 = 97.9340025$ are constant values of the Sellmeier equation.

We chose Au as the plasmonic material due to its chemical stability in aqueous environments and its significant change in the resonant wavelength (λ_{peak}) compared to other emerging nanometals. The permittivity of Au can be obtained using the Drude-Lorentz model, which is available directly from the COMSOL Multiphysics material library.

The sensor performance formulas can be expressed in Table 1.

Results and Discussions

Based on the FEM simulations, the structural parameters are provided in Table 2.

Figure 2 shows the real part of the RI for the core-guided mode (represented by the blue line) the SPP mode (represented by the red line), and the CL spectrum (depicted by the black curve). Using the geometric parameters listed in Table 2, the RI of the surrounding analyte is set to nana = 1.37.

In Fig. 2, the optical properties of the effective RI and CL for the x- and y-polarizations exhibit considerable similarity. The peak wavelength (λ_{peak}) is observed when the effective RI curve coincides with a high-order SPP mode. Under these conditions, energy is transferred from the guided core mode to the SPP mode, resulting in a CL peak at $\lambda_{peak} = 657$ nm for $n_{ana} = 1.37$.

Figure 3(a)–(c) depict the electric field distributions of the SPP and core-guided modes at the resonance wavelength (λ_{peak}) of 657 nm for the x- and y- polarizations. The illustrations clearly show the effective confinement of electric fields on the Au surface for the SPP mode and within the fiber core for the core-guided mode. Figure 3(a) shows that the SPR effect of the SPP mode is more pronounced on the four cutting edge surfaces than on the flat top and bottom surfaces of the Au film. This enhanced effect is attributed to the ability of surface plasmon resonance to intensify at sharp edges and corners. Therefore, this phenomenon facilitates the energy transition from the core region to the Au film.

Table 1 Formulas of sensor performance

Eq.	Formula	Remark
(2)	$\alpha \cong 8.686 \times \frac{2\pi}{\lambda} \times Im[n_{eff}] \times 10^4 \frac{dB}{cm}$	α is the CL of the core-guided [42, 43]. Here Im(n_{eff}) is an imaginary part of the effective RI
(3)	$S[nm/RIU] = \Delta\lambda_{peak}/\Delta n_{ana}$	S[nm/RIU] is the sensitivity. Where $\Delta\lambda_{peak}$ is the change in peak wavelength and Δn_{ana} denotes the shift in two successive RI
(4)	$R[RIU] = n_{ana} \times \frac{\Delta\lambda_{min}}{\Delta\lambda_{peak}}$	R[RIU] is the maximum theoretical resolution (MTR) [26, 44]. $\Delta\lambda_{min}$ is the wavelength resolution
(5)	$L = \frac{1}{\alpha(\lambda, n_{ana})}$	The length of the sensor is indicated as L(cm) [27]. Where $\alpha(\lambda, n_{ana})$ is the overall CL for a λ_{peak}.

Table 2 The structural parameters for the designed structure

r_1 (µm)	r_2 (µm)	r_3 (µm)	d_1 (µm)	d_2 (µm)	d_3 (µm)	t (nm)	h (nm)
0.8	0.7	0.4	1.8	1.5	2.25	25	75

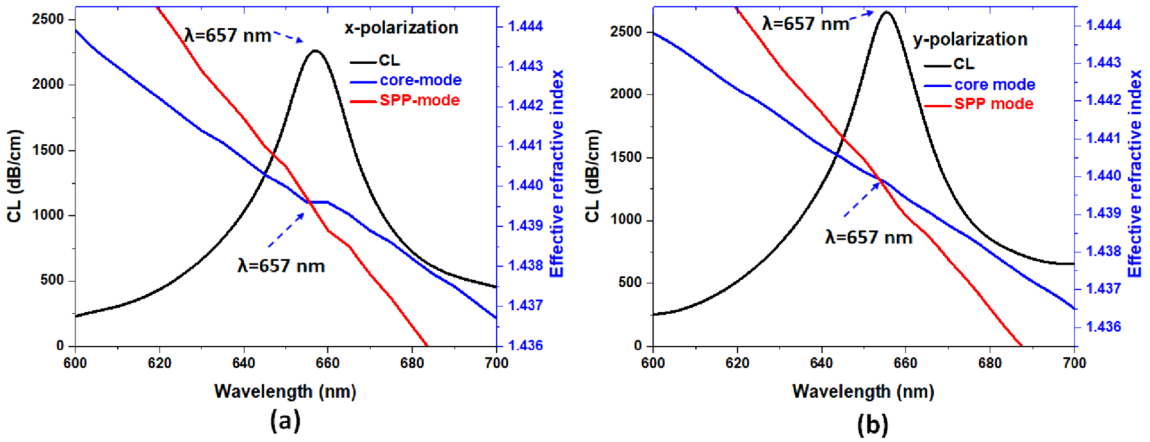

Fig. 2 **a** Real part of the RI for the core-guided mode (represented by the blue line), the SPP mode (represented by the red line), and **b** the CL spectrum (depicted by the black curve)

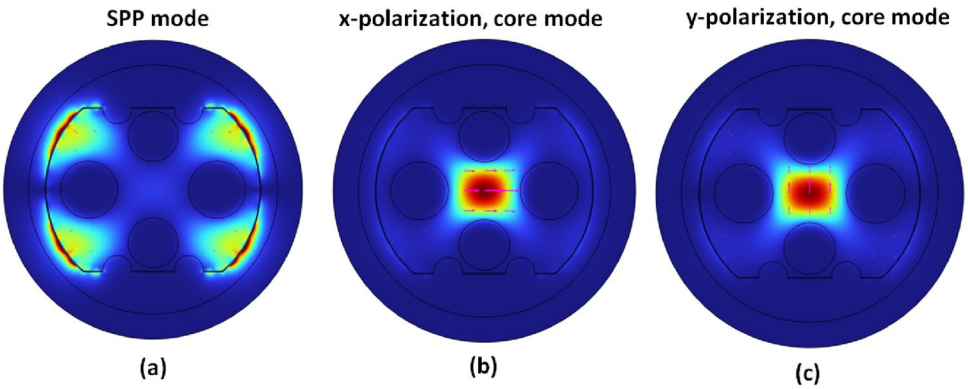

Fig. 3 E-field distributions at $\lambda_{peak} = 657$ nm: **a** SPP mode, **b** core mode for x-polarization, and **c** core mode for y-polarization

Crucial factors in the SPR-PCF sensor, which includes geometric parameters such as t, r_1, r_2, r_3 and h, influence the sensitivity of the designed structure. In subsequent simulations, we systematically inspect the geometric parameters shown in Table 1. Additionally, simulation results for the y-polarization are presented, as the results for both x- and y-polarizations are comparable in the proposed SPR-PCF. Furthermore, the variations in d_1, d_2, and d_3 have minimal impact on the simulation results; therefore, these values remain consistent, as listed in Table 2.

The value of t plays a crucial role in influencing the CL of the designed sensor. Variations in t strongly affect the change in the peak wavelength (λ_{peak}), providing a means to measure the interaction of the surface-coated testing medium with the external Au. FEM simulations (not presented here for simplicity) indicate a negligible CL peak due to the absence of the SPP effect when the outer surface of the SPR-PCF is not coated (i.e. $t = 0$ nm), rendering it nonfunctional for sensing purposes. However, as t increases from 10 to 50 nm (related to the skin of Au), significant changes in the expected sensor response [45, 46].

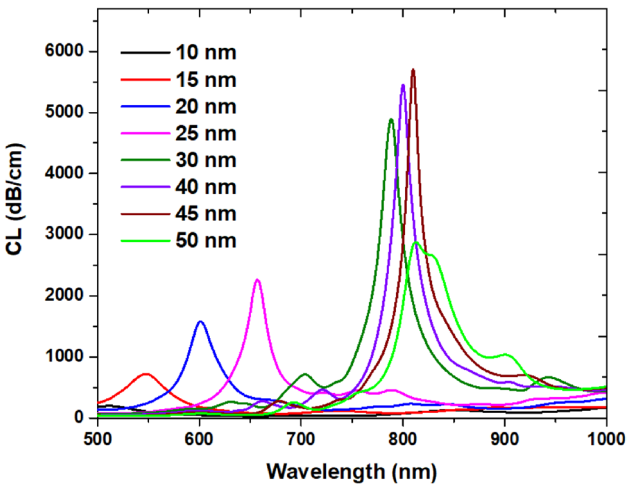

Fig. 4 CL spectra for various Au thicknesses, $t = (10, 15, 20, 25, 30, 40, 45, 50)$ nm

Figure 4 illustrates the CL spectra for different t that range from $t = 10$ nm to $t = 50$ nm. The other structural parameters, namely r_1, r_2, r_3, d_1, d_2, $d3$ and h, are set to 0.8, 0.7, 0.4, 1.8,

1.5, 2.25 µm, and 75 nm respectively. When t is 10 nm, the CL peak occurs at $\lambda_{peak} = 510$ nm, indicating a relatively low CL value compared to other values of t and a wide FWHM. This is attributed to a limited energy transfer from the fiber core region to the Au surface when t is relatively thin.

As t increases from 15, 20, 25, 30, 40 to 45 nm, the CL peak significantly redshifts, and the value of CL increases, with λ_{peak} shifting to 545 nm, 600 nm, 657 nm, 785 nm, 800 nm, and finally 810 nm, respectively. The corresponding CL values are 722.04, 1632.20, 2520.80, 4731.60, 5600.00, and 5700.92 dB/cm, respectively. This result suggests that the SPR effect can be adequately induced at a suitable Au thickness within this t range. The coupling effect between the fiber and Au films is enhanced, reaching its maximum value at $t = 45$ nm with $\lambda_{peak} = 810$ nm. However, when t increases to 50 nm, the coupling effect weakens due to the shielding of EM waves from the surface of the Au film, resulting in a decrease in the CL peak. Therefore, as t changes from 40 to 50 nm, the CL peak decreases from 5700.92 dB/cm to 815.28 dB/cm.

Figure 4 shows that it is the most crucial factor affecting the optical performance of the SPR-PCF. This can be explained by the matching impedance between the core and cladding regions of the fiber and the Au surface, as well as the SPR resonance conditions. When the resonance conditions of the fiber are met, variations in t lead to changes in impedance. Meanwhile, as the resonance conditions of the fiber change with t, λ_{peak} should increase to maintain impedance between the surface of the PCF and the Au film.

Based on the CL spectrum curves obtained from Fig. 4, Au thicknesses in the range of $t = (15, 20, 25, 30, 40, 45)$ nm can effectively serve as an SPR sensor, allowing manipulation of the desired peak wavelength depending on the t value. However, the CL spectrum curves for $t = (15, 20, 25)$ nm exhibit a lower CL peak wavelength and a higher FWHM, while those for $t = (30, 40, 45)$ nm show a higher CL peak wavelength and a narrower FWHM. This indicates that the optimal range of t can be selected from $t = (30, 40, 45)$ nm. We selected $t = 30$ nm as the optimal value to conserve Au material and consider the cost of the material.

The dimensions of the circular air holes and the half-curve at the flat planes play a crucial role in influencing the CL value, as they can alter the effective refractive index in the fiber cladding region. According to the FEM simulations, the dimensions of the air holes (r_1, r_2) and the half-curve (r_3) significantly affect the coupling effect to transfer energy between the core-guided mode and the surface plasmon polariton (SPP) mode.

Figures 5, 6, and 7 illustrate the CL versus wavelength for r_1, r_2 and r_3 ranging from 0.76 µm to 0.89 µm, 0.67 µm to 0.75 µm (withn increase of 0.1 µm), and 175 nm to 525 nm (with an increase of 25 nm), respectively. The other structural parameters, namely d_1, d_2, d_3, and t, h, are set to 0.8, 0.7, 0.4, 1.8, 1.5, 2.25 µm, 25 nm, and 75 nm, respectively. Furthermore, $r_3 = 0$ nm indicates flat planes without a half-curve in the top and bottom cases.

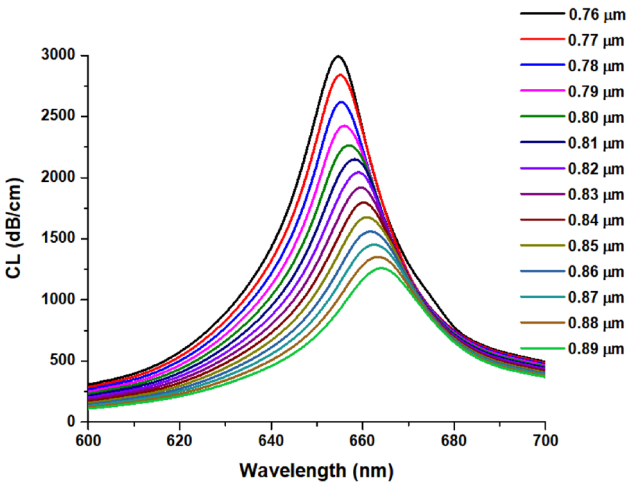

Fig. 5 CL spectra vary r_1 in the range of $0.76\ \mu m \le r_1 \le 0.89\ \mu m$ with an increase of 0.1 µm

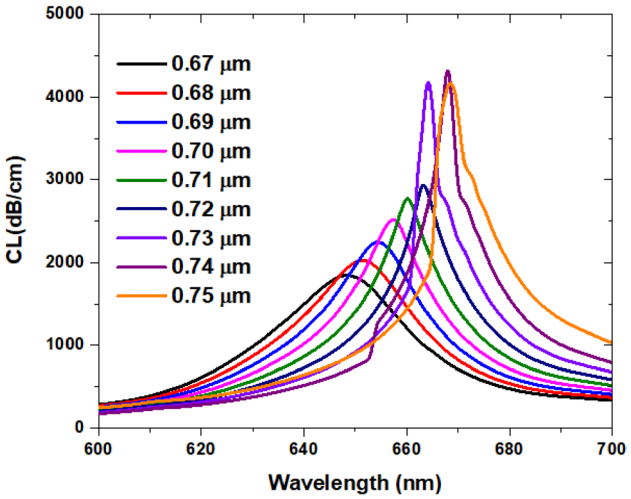

Fig. 6 CL spectra of r_2 in the range of $0.67\ \mu m \le r_2 \le 0.75\ \mu m$

Figure 5 presents CL spectra that vary r_1 in the range of 0.76 µm to 0.89 µm with an increase of 0.1 µm. CL peaks exhibit slight redshifts from $\lambda_{peak} = 655$ nm to 659 nm as r_1 increases from 0.76 µm to 0.89 µm, and the corresponding CL values decrease from 3077 dB/cm to 1311.00 dB/cm. The decrease in CL values with increasing r_1 is attributed to the larger air hole size, which reduces the effective RI in the fiber cladding, thus mitigating the coupling effect between the PCF and the external Au coating film.

It should be noted that the CL spectrum curves cannot exhibit a suitable SPR shape if r_1 is more significant than 0.89 µm or less than 0.76 µm based on FEM simulations (not

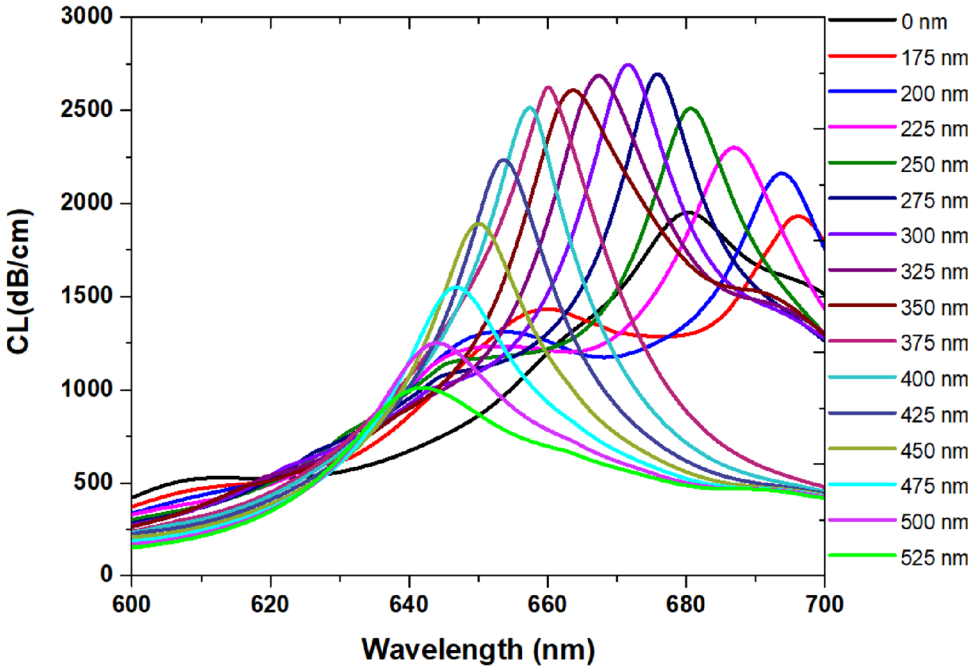

Fig. 7 CL spectra of $r_3 = 0$ nm and 175 nm $\leq r_3 \leq$ 525 µm with an increment of 25 nm of the proposed SPR-PCF structure

shown here for simplicity). Therefore, the suitable range of r_1 can be selected as 0.76 µm $\leq r_1 \leq$ 0.89 µm.

The size of r_2 can affect birefringence due to the different effective RI caused by the varying air sizes in the x- and y-directions, while maintaining the value of r_1. Figure 6 shows the CL spectra of r_2 ranging from 0.67 µm to 0.75 µm with an increase of 0.1 µm. Figure 6 shows that the CL peak undergoes a redshift and exhibits a higher value as r_2 increases within the range of 0.67 µm to 0.75 µm. These r_2 values apply to the designed device, indicating that we can manipulate the desired operating wavelength by adjusting r_2. The CL peaks show significant redshifts from $\lambda_{peak} = 648$ nm to 669 nm as r_2 varies from 0.67 µm to 0.75 µm, with the corresponding CL values increasing from 1845 dB/cm to 4190.00 dB/cm. The increase in CL values with increasing r_2 is attributed to the larger air hole size, which enhances the coupling effect between the fiber core and the external Au coating film, particularly under y-polarized light. In this scenario, we selected $r_2 = 0.73$ µm as the appropriate value, as it is acceptable CL (4340 dB/cm) and FWHM (15 nm).

The size of r_3 also significantly influences the CL value due to four half-curves (with a radius r_3) in the flat planes at the top and bottom, forming a dielectric window without Au coating. This results in different coupling effects between the two flat Au coating ends and the four air holes in the fiber cladding. Figure 7 illustrates the CL spectra for $r_3 = 0$ nm and the range of 175 nm $\leq r_3 \leq$ 525 nm (with an increase of 25 nm) for the proposed SPR-PCF structure. In Fig. 7, the black line represents the case ($r_3 = 0$ nm) without half curves on the surface of the upper and lower planes, which exhibits a low CL and a larger FWHM compared to the other cases with r_3 curves on the upper and bottom planar surfaces. This result is due to the reduced coupling effect between the PCF and the analyte when the half-curves are positioned at the top and bottom flat planes. For the other cases with half-curves in the flat planes of the top and bottom, the CL peaks undergo a blueshift from $\lambda_{peak} = 694$ nm to $\lambda_{peak} = 642$ nm as r_3 varies from 175 to 525 nm, with CL values ranging from 1395 dB/cm to 2960 dB/cm. The range of r_3 from 250 to 450 nm experiences higher CL values and a smaller FWHM (less than 20 nm) because this suitable range of r_3 speeds drives the EM wave away from the PCF to the Au film surface. We selected $r_3 = 400$ nm for the subsequent simulation based on an acceptable CL value (2520 dB/cm) and a smaller FWHM (13 nm).

The value of h significantly influences the CL value due to the gap between the air holes and the flat Au coating planes, which affects the coupling effect between the PCF ends and the air holes. Subsequently, we examine the various numbers of h. The other structural parameters, namely r_1, r_2, r_3, d_1, d_2, d_3, and t, are set to 0.8, 0.7, 0.4, 1.8, 1.5, 2.25 µm, and 25 nm, respectively. As depicted in Fig. 8, the CL spectrum experiences a redshift with increasing h in the 20–160 nm range. When h is in the range of 20 to 80 nm, it has a slight redshift from $\lambda_{peak} = 657$ nm to $\lambda_{peak} = 658$ nm, and the CL amplitude increases from 1713 dB/cm to 3257 dB/cm, decreasing to 2532 dB/cm when $h = 160$ nm. The FWHM enlarges with increasing h, which can be attributed to the reduced coupling effect between the surface plasmon polariton (SPP) mode of the Au coating plane and the core-guided mode of the air holes. The length of the Au-coated flat planes decreases with increasing h. These

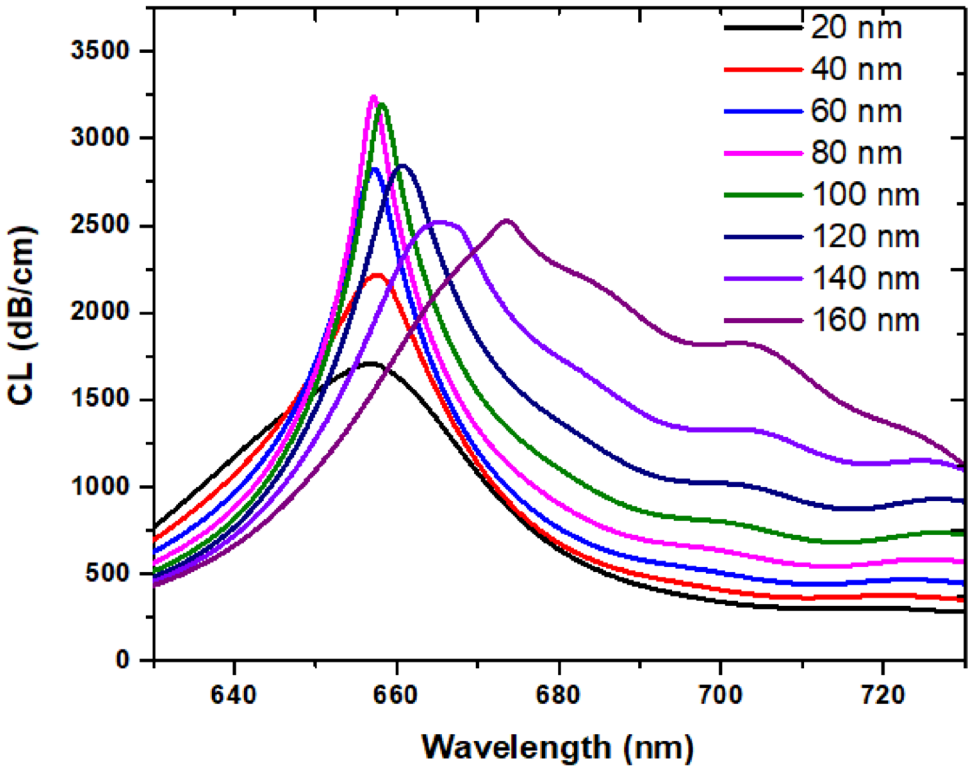

Fig. 8 CL spectra for 20 nm ≤ h ≤ 160 nm with an increment of 20 nm

Au-coated flat surfaces speed up the coupling effect between the PCF and the analytes, and the gold-coated flat length depends on h. According to the CL spectra, the available *h-range* can be chosen as 40–120 nm. We select $h = 80$ nm for subsequent simulations because it has a higher CL value and a smaller FWHM (10 nm).

Application of the RI Sensor

Finally, we examine the application of the designed RI sensor. Table 3 shows the optimal structural values based on Figs. 5, 6, 7, and 8.

We inspect the RI of the analyte, $n_{ana} = 1.30$, 1.31, 1.32, 1.33, 1.34, 1.35, 1.36, 1.37, 1.375, 1.38, 1.385, as the surrounding medium under test. Figure 9(a) and (b) present CL spectra for different RI values of the analytes (n_{ana}). Figure 9(a) shows results for n_{ana} ranging from 1.30 to 1.35 in increments of 0.01, while Fig. 9(b) shows results for $n_{ana} = 1.36$, 1.37, 1.375, 1.38, and 1.385. The CL amplitude is observed to increase with increasing n_{ana}, reaching a maximum value ranging from 202 dB/cm to 3655 when the n_{ana} varies from 1.30 to 1.375. Subsequently, CL decreases from 3655 dB/cm to 1600 dB/cm as the n_{ana} varies from 1.375 to 1.385. These CL values are proportional to Im(n_{eff}) based on Eq. (2). The maximum CL amplitude occurring at $n_{ana} = 1.375$ is attributed to the favorable resonance condition at this wavelength, which facilitates the coupling between the surface plasmon polariton (SPP) mode and the core-guided mode. The maximum n_{ana} value of 1.385 is selected in the proposed SPR PCF because no valid CL peak is observed when the $n_{ana} \geq 1.385$. In other words, for RI values of the target analyte ≥ 1.385, the λ_{peak} was not obtained, indicating that the proposed PCF cannot function as an SPR sensor when the $n_{ana} \geq 1.385$.

As shown in Fig. 9(a) and (b), with an increase in n_{ana}, all curves show a redshift. When the n_{ana} values are lower, the CL peak undergoes a shift; for example, when the n_{ana} changes from 1.30 to 1.36 with an increment of 0.01, the CL peak changes from 202 dB/cm to 1146 dB/cm. However, according to Eq. (2), as Im(n_{eff}) increases, the higher the value of nana, the faster the position change of the CL peak; for example, when n_{ana} increases from 1.37 to 1.375, the CL peak changes from 3655 dB/cm to 1660 dB/cm, and then

Table 3 Optimal structural values of the designed structure

r_1 (μm)	r_2 (μm)	r_3 (μm)	d_1 (μm)	d_2 (μm)	d_3 (μm)	t (nm)	h (nm)
0.78	0.73	0.4	1.8	1.5	2.25	30	80

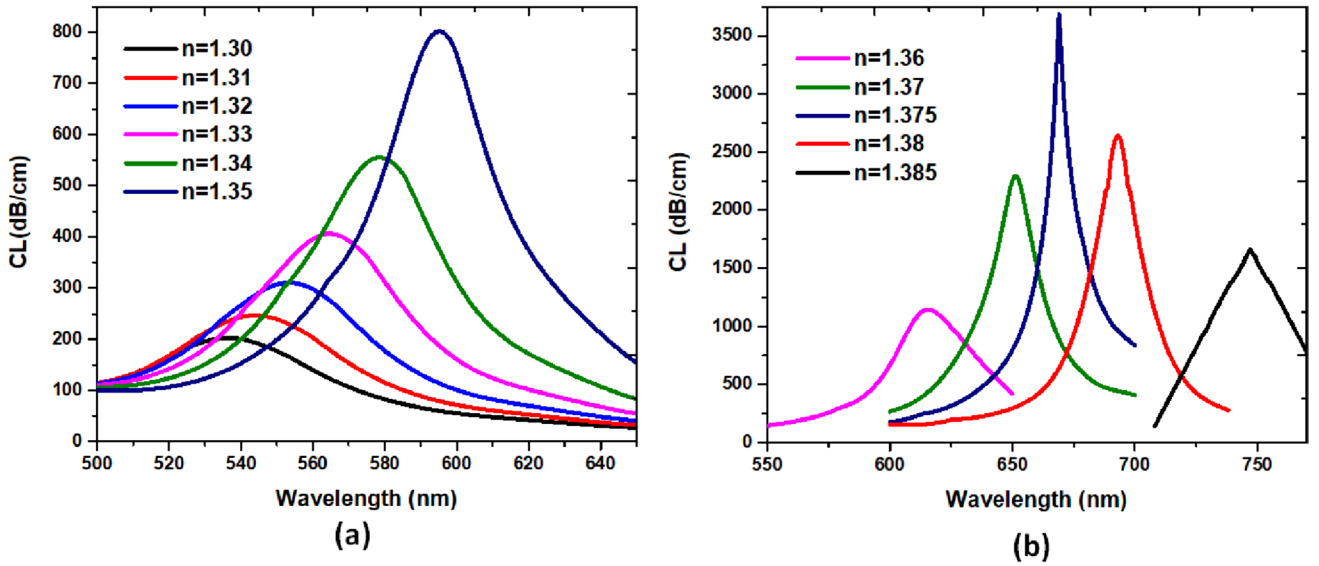

Fig. 9 CL spectra for different RI of analytes (n_{ana}), (**a**) n_{ana} = 1.30, 1.31, 1.32, 1.33, 1.34 and 1.35, (**b**) n_{ana} = 1.36, 1.37, 1.375, 1.38, and 1.385, respectively

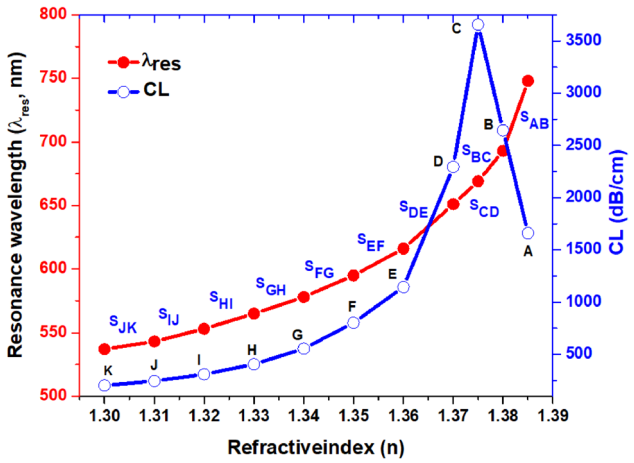

Fig. 10 λ_{peak} (nm) and CL spectra for different analytes (n_{ana}) with a range of 1.30–1.385

Table 4 The n_{ana}, CL (dB/cm), λ_{peak} (nm), L (cm), S (nm / RIU) and R for RIs ranges from 1.30 to 1.385

n_{ana}	CL (dB/cm)	λ_{peak} (cm)	L (cm)	S (nm/RIU)	R (RIU)
1.30	202	537	0.00495	NA	NA
1.31	246	543	0.00407	600	1.67×10^{-5}
1.32	310	553	0.00324	1,000	1.00×10^{-5}
1.33	406	565	0.00246	1,200	8.33×10^{-6}
1.34	555	578	0.00180	1,300	7.69×10^{-6}
1.35	803	595	0.00125	17,00	5.89×10^{-6}
1.36	1144	616	0.000874	2,100	4.76×10^{-6}
1.37	2295	651	0.000436	3,500	2.86×10^{-6}
1.375	3655	669	0.000274	3,600	1.39×10^{-6}
1.38	2645	693	0.000378	4,800	1.04×10^{-6}
1.385	1660	748	0.000602	11,000	4.54×10^{-7}

when n_{ana} increases from 1.375 to 1.385, the CL decreases from 2295 dB/cm to 3655 dB/cm. It should be noted that when $n_{ana} \geq 1.36$, the CL spectrum exhibits a noticeable redshift.

Figure 10 illustrates the λ_{peak} and CL spectra for different n_{ana} values within the range of 1.30 to 1.385. The sensitivity S can be determined by Eq. (2). As shown in Fig. 10, the S are S_{AB} = 11,000 nm/RIU, S_{BC} = 4,800 nm/RIU, S_{CD} = 3,600 nm/RIU, S_{DE} = 3,500 nm/RIU, S_{EF} = 2,100 nm/RIU in the wavelength range of 500 to 770 nm, respectively, S_{FG} = 1,700 nm/RIU, S_{GH} = 1,300 nm/RIU, S_{HI} = 1,200 nm / RIU S_{IJ} = 1,000 nm/RIU, and S_{JK} = 600 nm/RIU. For the S_{AB} case, the calculated figure of merit (FOM, defined by S_{AB}/FWHM) can obtain FOM = 220 1/RIU. The maximum theoretical resolution (MTR) of RI is expressed by Eq. (4). Δn_{ana} and $\Delta\lambda_{peak}$ in S_{AB} as shown in Fig. 10 are Δn_{ana} = 0.005 and $\Delta\lambda_{peak}$ = 55 nm, respectively. Assuming $\Delta\lambda_{min}$ = 0.1 nm, the achievable MTR is 9.09×10^{-6} RIU.

Table 4 presents the relevant data extracted from Fig. 10. This includes the n_{ana}, CL (dB/cm), λ_{peak} (nm), L (cm), S (nm / RIU) and R, corresponding to variations in refractive indices within the range of 1.30–1.385. Sensitivity increases with increasing n_{ana}, whereas length and resolution decrease with decreasing n_{ana}.

Table 5 compares a summary of the sensing performance, including the RI range, the number of air holes, the maximum S, L, and R, between the designed sensor and the

Table 5 Comparison of performance analysis between the designed structure and the previously reported sensors

Refs.	RI range	Number of air holes	Max. S (nm RIU^{-1})	R (RIU)
[47]	1.32–1.35	62	5,600	9.650×10^{-6}
[19]	around 1.33	55	4,950	2.0×10^{-5}
[48]	1.35–1.50	41	4,000	$2.94\,0 \times 10^{-5}$
[49]	1.32–1.38	40	5,500	1.82×10^{-5}
[50]	1.36–1.435	102	4,466	2.3×10^{-5}
[51]	1.415–1.427	74	10,250	N.A.
[52]	1.33–1.42	184	11,000	9.1×10^{-6}
This work	1.30–1.385	4	11,000	9.09×10^{-6}

previously published ones. It demonstrates that our designed structure exhibits excellent sensing performance with high sensitivity and better resolution while utilizing the minor air holes in the fiber cladding.

Conclusions

In conclusion, we have presented a simplified SPR-PCF sensor structure consisting of only four circular air holes coated with an Au layer on both polished and external PCF surfaces. Our proposed sensor demonstrates the capability to detect analytes externally. Through a comprehensive evaluation using the FEM in the COMSOL Multiphysics software, we have thoroughly assessed the sensing performance of this device and characterized its behavior. Our investigation has highlighted the significant influence of structural parameters such as t, r_1, r_2, r_3 and h on key sensor metrics including FWHM and CL amplitude. Optimizing these parameters, our proposed SPR-PCF sensor achieves a remarkable wavelength sensitivity of 11,000 nm/RIU, with a detection resolution of 9.09×10^{-6} RIU, observed for an analyte refractive index (RI) of 1.395. This level of sensitivity makes our device well suited for detecting highly active chemical and biological liquid samples. Furthermore, our sensor design stands out for its minimalistic approach, which incorporates the least number of air holes compared to articles reported in the literature. This simplicity streamlines fabrication processes and reduces costs, making our sensor a practical and cost-effective solution for high-sensitivity SPR-PCF sensing applications. Our study generally advances the SPR-PCF sensor technology by providing valuable theoretical insights. Our results underscore the superior sensing performance of our proposed SPR-PCF sensor, characterized by higher sensitivity and better resolution, achieved using the least air holes in the fiber cladding.

Author Contributions C.T.C.C: Writing-original draft preparation and simulations. M.U.A. H.J.H., C.M.L. and M.R.R.K.: Formal validation analysis and investigation. R.T. and Y.F.C.C.: Conceptualization, review, and editing. All authors reviewed the manuscript.

Funding This work was supported by the University Research Grant of Universiti Brunei Darussalam (Grant No. UBD/RSCH/URG/RG(b)/2023/036).

Data Availability Data will be made available on request.

Declarations

Ethics Approval There is no ethical approval required. Not applicable.

Consent to Participate Informed consent was obtained from all participants.

Consent to Publish Informed consent was obtained from all authors.

Conflicts of Interest The authors declare that they have no conflict of interest.

References

1. Deng Y, Cao G, Yang H, Zhou X, Yunwen Wu (2018) Dynamic Control of Double Plasmon-Induced Transparencies in Aperture-Coupled Waveguide-Cavity System. Plasmonics 13(1):345–352
2. Deng Y, Cao G, Yunwen Wu, Zhou X, Liao W (2015) Theoretical Description of Dynamic Transmission Characteristics in Mdm Waveguide Aperture-Side-Coupled with Ring Cavity. Plasmonics 10(6):1537–1543
3. Lin CT, Chang MN, Huang HJ, Chen CH, Sun RJ, Liao BH, Chau YF, Hsiao CN, Shiao MH, Tseng FG (2016) Rapid Fabrication of Three-Dimensional Gold Dendritic Nanoforests for Visible Light-Enhanced Methanol Oxidation. J Electrochimica Acta 192:15–21
4. Chau Y-F, Jiang Z-H, Li H-Y, Lin G-M, Fong-Lin Wu, Lin W-H (2011) Localized Resonance of Composite Core-Shell Nanospheres, Nanobars and Nanospherical Chains. Prog Electromagn Res B 28:183–199
5. Chau YF, Jheng CY, Joe SF, Wang SF, Yang W, Jheng SC, Sun YS, Chu Y, Wei JH (2013) Structurally and Materially Sensitive Hybrid Surface Plasmon Modes in Periodic Silver-Shell Nanopearl and Its Dimer Arrays. J Nanoparticle Res 15(3):1424
6. Chau YF, Din PT (2007) Three-Dimensional Analysis of Silver Nano-Particles Doping Effects on Super Resolution near-Field Structure. Opt Commun 269(2):389–94
7. Divya J, Selvendran S, Sivanantha Raja A, Sivasubramanian A (2022) Surface Plasmon Based Plasmonic Sensors: A Review on Their Past, Present and Future. Present and Future X 11:100175
8. Shangguan Q, Chen Z, Yang H, Cheng S, Yang W, Yi Z, Xianwen Wu, Wang S, Yi Y, Pinghui Wu (2022) Design of Ultra-Narrow Band Graphene Refractive Index Sensor. Sensors 22(17):6483
9. Chen H, Chen Z, Yang H, Wen L, Yi Z, Zhou Z, Dai Bo, Zhang J, Xianwen Wu, Pinghui Wu (2022) Multi-Mode Surface Plasmon Resonance Absorber Based on Dart-Type Single-Layer Graphene. RSC Adv 12(13):7821–7829
10. Zou H, Zhou J, Jiang A, Wei L, Yan Lu, Yuhang Du, Zhang R, Zhou D (2024) Ultra-Broadband Small-Size Dual-Core Photonic Crystal Fiber Polarization Splitter Based on Silver Coating. Opt Commun 557

11. Chau Y-F, Han-Hsuan Y, Din PT (2007) Significantly Enhanced Birefringence of Photonic Crystal Fiber Using Rotational Binary Unit Cell in Fiber Cladding. Jpn J Appl Phys 46(11L):L1048
12. Chau YF, Wu FL, Jiang ZH, Li HY (2011) Evolution of the Complete Photonic Bandgap of Two-Dimensional Photonic Crystal. Opt Express 19(6):4862–4867
13. Li T, Yan F, Xuemei Du, Wang X, Wang P, Suo Y, Zhou H, Kumamoto K (2023) Wavelength-Switchable Dual-Wavelength Thulium-Doped Fiber Laser Utilizing Photonic Crystal Fiber. Opt Communs 528
14. Mei C, Yuan Wu, Qiu S, Yuan J, Zhou X, Long K (2022) Design of Dual-Core Photonic Crystal Fiber for Temperature Sensor Based on Surface Plasmon Resonance Effect. Opt Commun 508:127838
15. Srivastava R, Pal S, Prajapati YK (2023) Mxene-Assisted D-Shaped Photonic Crystal Fiber Probe with High Sensitivity for Detection of Tuberculosis. Plasmonics 18(6):2049–58
16. Dandapat K, Tripathi SM (2021) Highly Sensitive Long-Period Fiber-Grating-Based Biosensor Inherently Immune to Temperature and Strain. J Opt Soc Am B 38(12):3601–07
17. Dandapat K, Saha N, Dwivedi R, Tripathi SM, Kumar A (2023) A Long-Period Waveguide Grating Sensor for Accurate Simultaneous Detection of Dual Analytes. IEEE Sens J 23(7):7059–7067
18. Haider F, Aoni RA, Ahmed R, Miroshnichenko AE (2018) Highly Amplitude-Sensitive Photonic-Crystal-Fiber-Based Plasmonic Sensor. J Opt Soc Am B 35(11):2816–21
19. Popescu V, Sharma AK, Marques C (2021) Resonant Interaction between a Core Mode and Two Complementary Supermodes in a Honeycomb Pcf Reflector-Based Spr Sensor. Optik 227
20. Tong K, Wang F, Wang M, Dang P, Wang Y (2018) Three-Core Photonic Crystal Fiber Surface Plasmon Resonance Sensor. Opt Fiber Technol 46:306–310
21. Wang D, Yi Z, Ma G, Dai Bo, Yang J, Zhang J, Yang Yu, Liu C, Xianwen Wu, Bian Q (2022) Two-Channel Photonic Crystal Fiber Based on Surface Plasmon Resonance for Magnetic Field and Temperature Dual-Parameter Sensing. Phys Chem Chem Phys 24(35):21233–21241
22. FFerdous AI, Kannan V, Logashanmugam E, Anwer TM, Anower S, Musha A, Kundu D, Sadeque G, Ahammad SH, Rashed AN, Hossain A, (2023) High-Sensitivity Pentagonal-Shaped Plasmonic Photonic Crystal Fiber for Sulfuric Acid Concentration Sensing. Plasmonics 18(6):2143–53
23. Khalaf MK, Taher HJ, Tahhan SR, Ahmed K, Al-Zahrani FA (2024)Design and Numerical Analysis of Refractive Index-Based Reproductive Hormone Sensor. Plasmonics. https://doi.org/10.1007/s11468-024-02208-5
24. Yan X, Wang Y, Cheng T, Li S (2021) Photonic Crystal Fiber Spr Liquid Sensor Based on Elliptical Detective Channel. Micromachines (Basel) 12(4):408
25. Islam MR, Iftekher AN, Hasan KR, Nayen MJ, Islam SB, Hossain A, Mustafa Z, Tahsin T (2021) Design and Numerical Analysis of a Gold-Coated Photonic Crystal Fiber Based Refractive Index Sensor. Opt Quantum Electron 53(2):112
26. Gao Di, Guan C, Wen Y, Zhong X, Yuan L (2014) Multi-Hole Fiber Based Surface Plasmon Resonance Sensor Operated at near-Infrared Wavelengths. Opt Commun 313:94–98
27. Han H, Hou D, Luan N, Bai Z, Song Li, Liu J, Yongsheng Hu (2020) Surface Plasmon Resonance Sensor Based on Dual-Side Polished Microstructured Optical Fiber with Dual-Core. Sensors 20(14):3911
28. Wang Q, Zhang X, Yan X, Wang F, Cheng T (2021) Design of a Surface Plasmon Resonance Temperature Sensor with Multi-Wavebands Based on Conjoined-Tubular Anti-Resonance Fiber. Photonics 8(6):231
29. Wang Y, Huang Q, Zhu W, Yang M, Lewis E (2019) Novel Optical Fiber Spr Temperature Sensor Based on Mmf-Pcf-Mmf Structure and Gold-Pdms Film: Erratum. Opt Letters 27(8):10813–10913
30. Rafi HN, Kaysir MR, Islam MJ (2020) Air-Hole Attributed Performance of Photonic Crystal Fiber-Based Spr Sensors. Sens Bio-Sens Res 29:100364
31. Rahman KM, Alam MS, Islam MA (2022) Highly Sensitive Gold-Coated Surface Plasmon Resonance Photonic Crystal Fiber Sensor in near-Infrared Region. Results Opt 7:100223
32. Li W, Jiang M, Jianjie Xu, Chen Yu, Zou H (2023) A Polished-D-Shape Spr-Based Photonic Crystal Fiber Sensor with High Sensitivity for Measuring Refractive Index. Photonics 13(8):1282
33. Majeed MF, Ahmad AK (2024) Design and Analysis of a High Sensitivity Open Microchannel Pcf-Based Surface Plasmon Resonance Refractometric Sensor. Opt Mater 147
34. Chang M, Li B, Chen N, Lu X, Zhang X, Xu J (2019) A Compact and Broadband Photonic Crystal Fiber Polarization Filter Based on a Plasmonic Resonant Thin Gold Film. IEEE Photonics J 11(2):1–12
35. Rifat AA, Mahdiraji GA, Chow DM, Shee YG, Ahmed R, Adikan FR (2015) Photonic Crystal Fiber-Based Surface Plasmon Resonance Sensor with Selective Analyte Channels and Graphene-Silver Deposited Core. Sensors 15(5):11499–510
36. Islam MS, Islam MR, Sultana J, Dinovitser A, Ng BW, Abbott D (2019) Exposed-Core Localized Surface Plasmon Resonance Biosensor. J Opt Soc Am B 36(8):2306–11
37. Steel MJ, Osgood RM (2001) Elliptical-Hole Photonic Crystal Fibers. Opt Letters 26(4):229–231
38. Sun YS, Chau YF, Yeh HH, Tsai DP (2008) Highly Birefringent Index-Guiding Photonic Crystal Fiber with Squeezed Differently Sized Air-Holes in Cladding. Jpn J Appl Phys 47(5R):3755
39. Yasli A, Ademgil H (2019) Effect of Plasmonic Materials on Photonic Crystal Fiber Based Surface Plasmon Resonance Sensors. Modern Phys Lett B 33(13):1950157
40. Chao CT, Chen SH, Huang HJ, Kooh MR, Lim CM, Thotagamuge R, Mahadi AH, Chau YF (2023) Improving Temperature-Sensing Performance of Photonic Crystal Fiber Via External Metal-Coated Trapezoidal-Shaped Surface. Curr Comput-Aided Drug Des 13(5):813
41. Yang KY, Chau YF, Huang YW, Yeh HY, Ping Tsai D (2011) Design of High Birefringence and Low Confinement Loss Photonic Crystal Fibers with Five Rings Hexagonal and Octagonal Symmetry Air-Holes in Fiber Cladding. J Appl Phys 109(9):093103
42. Wang D, Zhu W, Yi Z, Ma G, Gao X, Dai Bo, Yang Yu, Zhou G, Pinghui Wu, Liu C (2022) Highly Sensitive Sensing of a Magnetic Field and Temperature Based on Two Open Ring Channels Spr-Pcf. Opt Express 30(21):39055–39067
43. Isti MI, Talukder H, Islam SR, Nuzhat S, Hosen AS, Cho GH, Biswas SK (2020) Asymmetrical D-Channel Photonic Crystal Fiber-Based Plasmonic Sensor Using the Wavelength Interrogation and Lower Birefringence Peak Method. Results Phys 19:103372
44. Chiavaioli F, Gouveia CA, Jorge PA, Baldini F (2017) Towards a Uniform Metrological Assessment of Grating-Based Optical Fiber Sensors: From Refractometers to Biosensors. Biosensors 7(2):23
45. Zha F, Li J, Sun P, Ma H (2019) Highly Sensitive Selectively Coated D-Shape Photonic Crystal Fibers for Surface Plasmon Resonance Sensing. Phys Lett A 383(15):1825–1830
46. Chao CT, Kooh MR, Chau YF, Thotagamuge R (2022) Susceptible Plasmonic Photonic Crystal Fiber Sensor with Elliptical Air Holes and External-Flat Gold-Coated Surface. Photonics 9:916
47. An G, Hao X, Li S, Yan X, Zhang X (2017) D-Shaped Photonic Crystal Fiber Refractive Index Sensor Based on Surface Plasmon Resonance. Appl Opt 56(24):6988–6992
48. Chu S, Nakkeeran K, Abobaker AM, Aphale SS, Sivabalan S, Babu PR, Senthilnathan K (2020) A Surface Plasmon Resonance

Bio-Sensor Based on Dual Core D-Shaped Photonic Crystal Fibre Embedded with Silver Nanowires for Multisensing. IEEE Sens J 21(1):76–84
49. Chen N, Chang M, Xinglian Lu, Zhou J, Zhang X (2019) Photonic Crystal Fiber Plasmonic Sensor Based on Dual Optofluidic Channel. Sensors 19(23):5150
50. Liu E, Yan B, Zhou H, Liu Y, Liu G, Liu J (2021) Oam Mode-Excited Surface Plasmon Resonance for Refractive Index Sensing Based on a Photonic Quasi-Crystal Fiber. J Opt Soc Am B 38(12):F16–F22
51. Li C, Yan B, Liu J (2019) Refractive Index Sensing Characteristics in a D-Shaped Photonic Quasi-Crystal Fiber Sensor Based on Surface Plasmon Resonance. J Opt Soc Am A 36(10):1663–1668
52. Rifat AA, Haider F, Ahmed R, Mahdiraji GA, Adikan FM, Miroshnichenko AE (2018) Highly Sensitive Selectively Coated Photonic Crystal Fiber-Based Plasmonic Sensor. Opt Lett 43(4):891–94